Applied Energy 369 (2024) 123478

Contents lists available at ScienceDirect

Applied Energy

journal homepage: www.elsevier.com/locate/apenergy

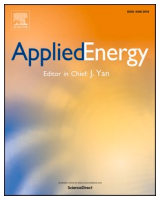

The advantage of running a direct expansion CO_2 heat pump with solar-and-air simultaneous heat sources: experimental and numerical investigation

Riccardo Conte [a], Emanuele Zanetti [a,b], Marco Tancon [a], Marco Azzolin [a,*], Sergio Girotto [c], Davide Del Col [a]

[a] Department of Industrial Engineering, University of Padova, Via Venezia 1, 35131 Padova, Italy
[b] Department of Process and Energy, Delft University of Technology, Leeghwaterstraat 39, 2628 CB Delft, the Netherlands
[c] ENEX S.r.l., Vacil di Breda di Piave (Treviso), 31030, Italy

HIGHLIGHTS

- A dual source CO2 heat pump with PV-T evaporators has been experimentally investigated.
- The simultaneous use of the two evaporators adds more flexibility to the system and its design.
- The availability of a small solar area can contribute enhancing the performance over the mere air source.
- A dynamic numerical model of the heat pump has been realized in Matlab environment.
- The model is used to study the heat pump's performance varying solar irradiance and number of collectors.

ARTICLE INFO

Keywords:
Dual-source heat pump
PV-T
Air source
Direct expansion
Carbon dioxide
Flooded evaporator

ABSTRACT

Dual-source solar-air heat pumps represent a promising solution for overcoming the limitations associated with single-source utilization, thereby enhancing heat pump performance. However, running the heat pump by alternatively employing the more advantageous source requires the integration of a controller capable of continuously monitoring and predicting the heat pump's performance in response to dynamic environmental and operational variables. Even so, a selective alternate operation does not allow to get the maximum possible performance from the use of the two heat sources. A different approach to address this challenge is the simultaneous utilization of the two sources, by properly combining two evaporators in the CO_2 circuit. This paper presents an experimental investigation of a dual-source heat pump using CO_2 as refrigerant, which can operate in three different evaporation modes: air-mode (using a finned-coil evaporator), solar-mode (using a photovoltaic-thermal PV-T evaporator), and simultaneous-mode (using both the evaporators simultaneously). The novel solution presented here does not require to split the refrigerant flow rate between the two evaporators and at the same time it solves the problem of possible maldistribution at the inlet of the evaporators. Experimental data indicate that the heat pump operating in simultaneous-mode allows to increase the evaporation pressure and the coefficient of performance compared to operation in air-mode or solar-mode. The measurements have been employed for validating a model of the system, capable of predicting steady-state and dynamic performance under various environmental and operational conditions. Simulation results show that the simultaneous-mode operation can be outperformed by the solar-mode only at high irradiance and low air temperature, when the evaporation temperature gets higher than the air temperature. Finally, the impact of the number of PV-T collectors and solar irradiance on the heat pump performance has been simulated and discussed. On this regard, the simultaneous use of the two heat sources adds more flexibility to the system and its design, because even the availability of a small solar area can contribute enhancing the performance over the mere air source heat pump.

* Corresponding author.
E-mail address: marco.azzolin@unipd.it (M. Azzolin).

https://doi.org/10.1016/j.apenergy.2024.123478
Received 14 February 2024; Received in revised form 9 April 2024; Accepted 13 May 2024
Available online 31 May 2024

1. Introduction

Air source heat pump (ASHP) stands out as an extensively employed heating system in buildings, offering benefits such as straightforward installation, low energy consumption, significant energy-saving capabilities, and environmental-friendly characteristics [1]. Nonetheless, the ASHP performance is reduced when the air temperature decreases. Additionally, low air temperature and high relative humidity can lead to frost formation on the outdoor finned coil evaporator's surface. Kropas et al. [2] observed experimentally that when the relative humidity reached about 90% and the air temperature dropped below 3 °C, frost began to form on the finned coil evaporator. In these conditions, the frost and defrost process reduced the coefficient of performance (COP) of the ASHP by 11% compared to its normal operation without frost formation. This performance reduction occurred due to the increased heat transfer and airflow resistance resulting from accumulated frost during operation, leading to system degradation or potential shutdown. Large experimental and theoretical analyses have been conducted on ASHP system to analyze their operational efficiency in scenarios involving frosting and defrosting [3].

A possible alternative to ASHPs is the application of solar-assisted heat pumps (SAHPs), which are capable of exploiting solar irradiance as heat source [4]. The SAHPs can be of two types:

1. Indirect solar-assisted heat pump (IDX-SAHP), in which solar radiation is captured by water-driven solar collectors and the heated water is subsequently directed to the evaporator;
2. Direct solar-assisted heat pump (DX-SAHP), in which solar radiation is absorbed directly by refrigerant-driven solar collectors, serving as the evaporators.

The majority of research on SAHP is concentrated on indirect systems. IDX-SAHP represents a well-established technology in the market, with recent scientific investigations focusing on their integration into buildings and their long-term operational efficiency [5]. However, despite their complexity, DX-SAHPs eliminate the need for water pumps and intermediate heat exchangers, avoiding large temperature drops in the collectors, due to the isothermal evaporation process. Additionally, the use of refrigerant as the thermal carrier mitigates potential risks of freezing and corrosion within the collectors [6]. Several solar collector technologies have been experimentally tested as evaporators in DX-SAHPs. The most common are the flat-plate or roll-bond [7–9] but a recent study analysed also the evacuated tubes [10].

Using photovoltaic-thermal (PV-T) collectors as solar evaporators is another innovative strategy to increase SAHPs efficiency [11,12]. Despite their lower thermal efficiency compared to conventional solar thermal collectors, the advantage of PV-T panels becomes evident when considering overall net consumption, due to the electrical production given by the cooled PV cells. Several studies have demonstrated that is possible to fully meet the heat pump electricity demand with photovoltaic production in SAHP employing PV-T [13,14].

As mentioned above, the efficiency of the ASHP and SAHP is reduced when air temperature and solar irradiance are low, respectively. Therefore, to enhance the heat pump performance, an alternative approach is to combine the two sources. Simonetti et al. [15] studied an energetic and economic evaluation of three distinct SAHPs working with R410A in a single-family house: (a) a ASHP combined with PV, (b) a IDX-SAHP connected to PV-T collectors and (c) a dual-source heat pump (DSHP) with PV-T collectors in indirect configuration. The results indicate that the ASHP has the lowest running cost and the highest saving, while the DSHP has the highest energy efficiency. However, using a DSHP presents the challenge of efficiently managing the switch between the two sources to maximize the performance of the system, as presented in [14] for a solar-air dual-source heat pump (SA-DSHP). Li et al. [16] experimentally and numerically showed that SA-DSHP, in indirect configuration, improves both technical and economic performance compared to ASHP, during heating season. Forcing the use of the external source in a DSHP means that there should be a control system with a specific algorithm developed to choose which heat exchanger has to operate depending, for instance, on the thermal load, air temperature, humidity and solar irradiance. For this reason, it has been shown that it is possible to run the two sources at the same time, as recently highlighted by Li et al. [17], which showed that single-phase solar thermal collectors can operate simultaneously with the heat pump system, in series (as pre-heaters), in parallel, or in SA-DSHP configuration, where the solar thermal collectors supply the water-to-refrigerant evaporator. In the specific case of direct SA-DSHPs, when air and solar evaporators are integrated into the heat pump, two configurations can be found:

1) parallel configuration: the refrigerant mass flow rate is split between the solar and the air evaporators when they work simultaneously;
2) series configuration: the same refrigerant mass flow rate feeds the solar and air evaporators sequentially.

Deng et al. [18] conducted a numerical investigation of a SA-DSHP that utilized a solar collector and a finned coil evaporator in parallel configuration. It was found that the SA-DSHP resulted in a significant performance improvement, especially under low solar irradiance. At an air temperature of 20 °C and a solar irradiance of 100 W m^{-2}, the average COP of the SA-DSHP (4.46) was about 14% higher as compared to the DX-SAHP. Li and Huang [19] developed a mathematical model to compare the performance of a SA-DSHP employing an air evaporator and a PV-T collector in parallel configuration with a DX-SAHP and an ASHP. Their results demonstrate that the SA-DSHP exhibits enhanced heating capacity and system COP in challenging environments characterized by low solar irradiance and air temperature compared to the DX-SAHP and ASHP. In addition, the SA-DSHP achieves improved performance with a reduced PV-T surface area. Li et al. [20] numerically investigated the use of an ejector to enhance the performance of a SA-DSHP equipped with two evaporators in parallel configuration: a finned coil and PV-T collectors. The results showed that this configuration outperforms the ASHP, increasing the COP by 26% at the design conditions when using R134a as refrigerant.

The major drawback of using evaporators in parallel configuration is related to the maldistribution of the refrigerant flow rate among the different evaporators. Cai et al. [21] studied an innovative SA-DSHP with a finned coil and a solar evaporator in series. The proposed system achieves the maximum COP enhancement when working at 200 W m^{-2} of solar irradiance and air temperatures ranging from 10 to 30 °C, as compared to DX-SAHP and ASHP. Subsequently, the authors compared different configurations of the hybrid heat pump [22]: solar-air in series (two possible configurations depending on the order of the evaporators) and solar-air in parallel. Model results show that the configuration with the air evaporator positioned after the solar collector is well suited for operation at low solar irradiation, whereas the parallel configuration can achieve optimal performance at high solar irradiation or high air temperature. Yang et al. [23] conducted a numerical study on a SA-DSHP with PV-T collectors in series configuration with a switchable finned coil evaporator, which can meet both heating and cooling demand. The results indicated that the electrical efficiency of cooled PV panels was higher than that of uncooled PV panels, with an increase in the range 4.1%–13.7% in winter and 1.1%–10.6% in summer. Zhang et al. [24] numerically investigated a SA-DSHP with a finned coil and an innovative PV-T collector in series configuration. The novel PV-T collector employs micro-channel heat pipe and double-circuit to control the heat transfer direction of refrigerant. This allows the refrigerant to absorb heat from the photovoltaic system during heating cycles while preventing heat release to the photovoltaic system during cooling cycles. The authors explained that the finned coil evaporator shares the heat absorption or dissipation and the pressure of the PV-T collector. This cooperative interaction contributes to the stability of the system during

both cooling and heating modes.

From this literature review, it emerges that studies dealing with the simultaneous use of solar and air evaporators in parallel and series configuration are limited, and most of them are numerical. Furthermore, there is a lack of experimental data for SA-DSHP systems, where the evaporators can operate either alternatively or simultaneously, and where the solar collectors are PV-T. In addition, none of the previous studies have addressed the potential issue of maldistribution that can occur when a multi-circuit evaporator is supplied with a mixture of vapor and liquid, as in the case of solar evaporators located after a finned coil heat exchanger.

It is also worth mentioning that the majority of studied DX-SAHP systems adopts HCFC and HFC as refrigerants. Among them, R134a is the most commonly used HFC [12], with a few studies exploring R32 [25] and R410A [26]. Only one existing prototype employs a natural refrigerant, specifically CO_2 [27]. It emerges that there is a lack of experimental works involving natural refrigerants in DSHP operating with both air and solar evaporators. It should be considered that the use of natural refrigerants in the future heat pumps will hold significant importance in light of recent regulations, as the European Union's F-gas Regulation (EU) 2024/573 [28], which aims to phase down the use of HFCs in the European Union. Compared to heat pump systems that use other refrigerants, CO_2 has the advantage of reducing the size of the compressor and pipeline due to its high density, as well as the size of the heat exchangers due to its superior flow and heat transfer properties [29]. Another benefit is that CO_2 reduces its temperature without phase change during heat transfer on the high-pressure side, allowing a higher secondary fluid temperature to be achieved. Hydrocarbons, such as propane, are the only other natural fluid alternative to CO_2 for heat pump applications. However, in such systems, with solar evaporators and not self-contained, hydrocarbons must be excluded due to their high flammability. In conclusion, heat pumps for the simultaneous usage of two evaporators, one for the solar radiation and the second for the air source, has to be considered subject for new research.

The aim of this work is to present a prototype of a CO_2 SA-DSHP which uses two evaporators and can work either with the two sources simultaneously or with a single source. The configuration of the simultaneous use of the two evaporators is completely new, it is not a parallel nor a series one. The two evaporators consist of a finned coil heat exchanger for the air source and three PV-T collectors for the solar source. The latter are designed to work in a flooded configuration, meaning that they are supplied by liquid CO_2 through a specifically designed loop, eliminating the issue of maldistribution. This flooded loop is independent from the main circuit.

In the present paper, the heat pump operation with the simultaneous use of the two evaporators is compared with the single source operation modes, and a simple method for switching between the operative modes has been presented. A numerical model has been employed to evaluate the heat pump performance when working in steady-state conditions but also in dynamic conditions. The model allows to evaluate the impact of weather conditions and solar collector's area on the heat pump performance in the various evaporation modes. These results are important because they show the flexibility of the presented system, leading to a performance increase over the mere ASHP even with a small available collector area.

Finally, the choice of PV-T collectors instead of normal solar collectors as evaporators is made with two purposes: limit the needed solar area, because PV-T collectors can be installed in place of normal PV panels, and reduce the PV cell temperature during evaporation, improving the electrical conversion efficiency.

2. Experimental methods

The present prototype is a SA-DSHP using CO_2 as refrigerant and it is installed at the Department of Industrial Engineering of the University of Padova (latitude 45.41, longitude 11.89). Two evaporators are installed to exploit solar and air as low-temperature thermal sources: three photovoltaic-thermal (PV-T) solar collectors and a conventional finned coil heat exchanger, respectively. The SA-DSHP can operate either with one of the two types of evaporators or with both evaporators at the same time. It is worth stressing that the PV-T collectors serve as heat pump evaporators because the refrigerant flows directly in the PV-T tubes. The maximum heating capacity of the CO_2 heat pump is equal to 5 kW and hot water is produced at the gas-cooler operating a transcritical cycle. Fig. 1 shows a front view of the SA-DSHP prototype.

2.1. Description of the experimental facility

The system layout of the SA-DSHP prototype, including the measurement sensors, is displayed in Fig. 2. In particular, the design of the refrigerant loop is such that the SA-DSHP can be operated in three modes (indicated by black lines) following the evaporation mechanism:

a) Air-mode (AIR-M);
b) Solar-mode (SOL-M);
c) Simultaneous-mode (SIM-M).

Regarding the common part of the layout, the compressor (labelled COMP) brings the superheated vapor-phase refrigerant from the evaporating pressure to the high-pressure side. The gas-cooler (GC) is utilized to heat the water flowing on the secondary side. After the GC, the refrigerant flows into an internal heat exchanger (IHE), where it cools and is then expanded in an electronic expansion valve (EEV). The EEV acts as a backpressure valve, adjusting the aperture to fix the high-pressure level and it is controlled with an external 0–10 Vdc signal.

When considering the AIR-M operation (Fig. 2a), the low-temperature thermal source is the air. Therefore, after the EEV, the refrigerant enters the finned coil evaporator and then the low-pressure receiver (REC) before returning to the compressor.

When considering the SOL-M operation (Fig. 2b), the heat pump exploits the solar irradiance as thermal source. In this configuration, the two-phase refrigerant is not sent directly to the evaporator after the EEV. Instead, it first goes to the REC. The liquid CO_2 is then extracted from the bottom and pumped, through a circulation pump (PUMP), to the three PV-T collectors, connected in parallel. Therefore, the evaporator operates in flooded configuration with forced circulation. After the evaporation process in the PV-T collectors, the refrigerant returns to the REC, closing the loop. In this way, it is possible to decouple the refrigerant flow rate circulating in the collectors and driven by the pump from that circulating in the main loop and driven by the compressor.

In SIM-M operation (Fig. 2c), the SA-DSHP can exploit both the solar irradiance and the air as low-temperature thermal sources at the same time. This is a combination of the previous operation modes and it is composed of two steps. After the EEV, the refrigerant flows to the finned coil heat exchanger where it partially evaporates (first step). Then, the refrigerant flows into the REC where the liquid CO_2 is extracted from the bottom and circulated to the PV-T collectors where it vaporizes (second step). The finned coil, the PV-T collectors and the REC are at the same pressure level. In this operation mode, the two evaporators work simultaneously. This refrigerant loop configuration avoids the problem of properly feeding with CO_2 both the finned coil evaporator and the PV-T collectors. This aspect represents a major novelty contribution of the present study.

In all the operative modes, between the REC and the suction line of the compressor, the CO_2 flows through the IHE, which is used to superheat the refrigerant before it enters the compressor. To adjust the degree of superheating, a three-way valve (VB) is used to by-pass a portion of the total refrigerant flow rate coming from the REC.

2.2. Components

The COMP is an inverter-driven hermetic vertical rotary compressor

Fig. 1. Pictures of the SA-DSHP prototype with details of the finned coil and of the back view of a PV-T collector.

with a single rotary (model DY30N1F-10FU by Toshiba, displacement of 3.02 cm^3 rev^{-1}) and lubricated with PAG oil VG100. The GC and the IHE are brazed plate heat exchangers, both in a single pass/counterflow configuration. The GC has 28 plates with dimensions of 379 × 79 mm^2, while the IHE has 4 plates with dimensions of 377 × 120 mm^2. The circulation pump of the liquid CO_2 in the PV-T collectors is a variable-speed magnetically driven gear pump (MICROPUMP model GC-M23) with a displacement equal to 0.81 mL rev^{-1}. The maximum processed volumetric flow rate is 2310 mL min^{-1} at 2850 rpm and 50 Hz. The solar evaporator comprises three PV-T collectors, where the photovoltaic modules are coupled at the back to a plate-and-tube heat exchanger. The PV-T collectors allow both the evaporation of the refrigerant flow and the cooling of the photovoltaic cells, thereby enhancing photovoltaic power production (see [14]). The PV modules are composed by multi-crystalline silicon cells with 270 W nominal power and a gross area equal to 1.64 m^2 each (dimensions 1650 × 992 mm^2). The PV modules are electrically connected in series and, for this study, the generated power is dissipated to a wirewound rheostat. This allows the electrical load to be varied and the maximum power point (MPPT) to be tracked manually. The plate-and-tube heat exchanger consists of 15 copper tubes serpentine (8 mm outer diameter and 1 mm thickness) with a pith of 80 mm, welded on an aluminium absorber plate (0.5 mm thickness). The present aluminium plate area covers 75% of the useful space available on the back sheet of the photovoltaic module and it has been applied using a thermal adhesive. The PV-T collectors are installed with a tilt angle equal to 45°. The air evaporator is a finned coil heat exchanger. It consists of 4 circuits of copper tubes (10.12 mm outer diameter and 0.35 mm thickness), distributed in 4 rows and 22 ranks with 21.65 mm row spacing and 25 mm tube spacing. The aluminium fins have 0.12 mm thickness and 3.2 mm spacing. A variable-speed fan (350 mm diameter) is coupled to the finned coil and its rotation speed is modulated by a 0–10 Vdc signal. The maximum airflow is 2350 m^3 h^{-1} at 1400 rpm, with a power consumption of 180 W. The main characteristics of the heat pump's components are reported in Table 1.

The SA-DSHP is equipped with several sensors, as shown in the schematic of Fig. 2, to monitor its main performance indicators. The temperature and pressure values of the refrigerant in the loop are monitored using T-type thermocouples (symbol T in Fig. 2) and pressure transducers (symbol P in Fig. 2). Each thermocouple has been calibrated against Fluke® 1586 A Super-DAQ Precision Temperature coupled with a 1/10 DIN Pt 100 probe. After the calibration procedure, the deviations between thermocouple measurements and reference are within ±0.1 K. The environmental conditions are acquired using a RTD (Pt-100) for air temperature, a cup anemometer for the velocity and three pyranometers for the different components of solar radiation. In particular, the global tilted irradiance on the collector plane and the global horizontal irradiance are recorded using two Kipp and Zonen CM11 pyranometers, whereas the diffuse horizontal irradiance is quantified utilizing a Kipp and Zonen CMP22 pyranometer fitted with a shading ring. The pyranometers are secondary standard according to the ISO 9060 classification system [37]. In the GC, the water inlet/outlet temperatures and the water mass flow rate are measured by means of two platinum resistance thermometers Pt-100 and a Coriolis effect flow meter (CFM in Fig. 2), respectively. The total electric power consumption of the heat pump (including the fan, if used), the compressor power consumption (including the inverter) and the power produced by the PV modules are measured by a power analyzer Norma 4000.

2.3. Data reduction

The COP is calculated as the ratio of the heat flow rate rejected at the gas-cooler (Q_{GC}) to the electrical power consumption. Two different COPs can be defined: COP_c considers only the compressor electrical power consumption (P_c); COP_{tot} considers the total electrical power consumption (P_{tot}), including the compressor, the finned-cooled evaporator fan, the PV-T evaporator pump and the heat pump electronics:

$$COP_c = \frac{Q_{GC}}{P_c} \tag{1}$$

$$COP_{tot} = \frac{Q_{GC}}{P_{tot}} \tag{2}$$

where Q_{GC} is determined by the energy balance on the water-side, knowing the mass flow rate ($\dot{m}_w$), the specific heat capacity (c_w) and the inlet/outlet temperature ($T_{in,w}$ and $T_{out,w}$):

$$Q_{GC} = \dot{m}_w c_w \left(T_{in,w} - T_{out,w}\right) \tag{3}$$

The refrigerant mass flow rate is determined by the energy balance on the refrigerant-side, knowing the inlet/outlet refrigerant specific enthalpies ($h_{in,GC}$ and $h_{out,GC}$):

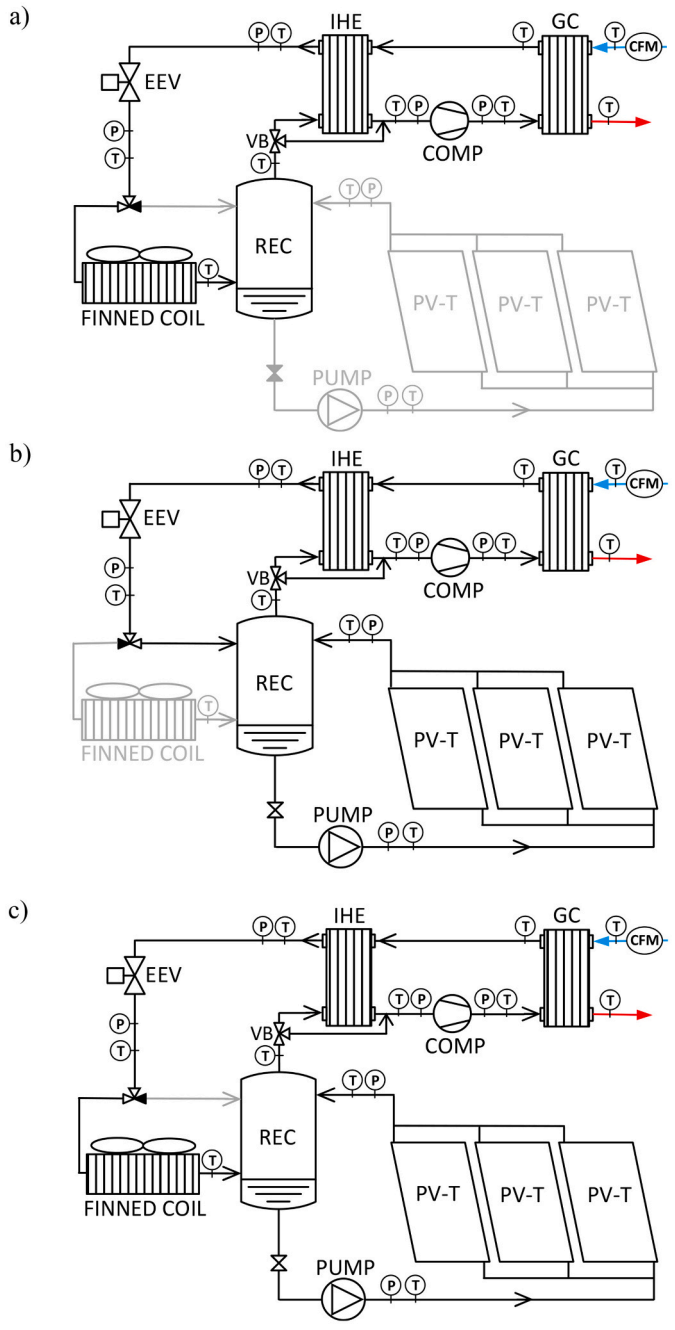

Fig. 2. Scheme of the SA-DSHP prototype and the refrigerant loop (black line) in a) AIR-M, b) SOL-M and c) SIM-M. The picture shows the temperature (T), pressure (P) and flow rate (CFM) sensors.

$$\dot{m}_r = \frac{Q_{GC}}{h_{in,GC} - h_{out,GC}} \tag{4}$$

The evaporation heat flow rate of the is calculated, regardless of the evaporator type, by performing an energy balance that considers the enthalpies at the outlet of both the EEV and of the REC:

$$Q_{EVAP} = \dot{m}_r \left(h_{out,EEV} - h_{out,REC}\right) \tag{5}$$

where the enthalpy at the EEV outlet ($h_{out,EEV}$) is calculated assuming an isenthalpic expansion:

$$h_{out,EEV} = h_{in,EEV} \tag{6}$$

where $h_{in,EEV}$ is the EEV inlet specific enthalpy.

Table 1
Main components of the heat pump and their characteristics.

Component	Type	Characteristics
Compressor	Rotary, inverter driven	Displacement: 3.02 cm^3 rev^{-1}
Gas-cooler	Brazed plate	Plate size: 379 × 79 mm^2 N° of plates: 28
Internal heat exchanger	Brazed plate	Plate size: 377 × 120 mm^2 N° of plates: 4
Throttling valve	Electronic	High-pressure control
Receiver	Cylindrical tank	Tank size: 20 L
Air evaporator	Finned coil	N° of circuits: 4 N° of tubes: 88 Tube diameter (internal): 9.5 mm
PV module	Multicrystalline silicon	N° of modules: 3 Nominal power: 270 W Dimensions: 1650 × 992 mm^2
Solar evaporator	PV-T collectors	Plate-and-tube heat exchanger Plate area: 75% of PV area Tube diameter (internal): 6 mm
Circulation pump	Gear pump, variable-speed	Displacement: 0.81 mL rev^{-1}

The evaporation temperature is calculated from Refprop 10 [30] by knowing the saturation pressure gauged at the outlet of the PV-T collectors (see Fig. 2).

The IHE heat flow rate is derived by applying the energy balance at the high-pressure side:

$$Q_{IHE} = \dot{m}_r \left(h_{out,GC} - h_{int,EEV}\right) \tag{7}$$

The thermal efficiency of the PV-T collectors is:

$$\eta_{th} = \frac{Q_{EVAP}}{GTI \cdot A} \tag{8}$$

where A is the aperture area of the collector and GTI is the global tilted irradiance.

The refrigerant enthalpies are estimated from temperature and pressure measurements using NIST Refprop 10.0 [30]. The uncertainty analysis was conducted according the JCGM guidelines [31]. The type B uncertainty values and the average combined uncertainties of main calculated parameters are reported in Table 2.

2.4. Experimental conditions

The experimental tests presented in this study were carried out during winter environmental conditions. Measurements were conducted under both steady-state and transient conditions across a range of compressor speeds. In the secondary loop, both the $\dot{m}_w$ and $T_{in,w}$ were controlled. This was done to achieve a fixed $T_{in,w}$ between 30 °C and 31 °C and an inlet/outlet temperature difference of 5 K, in accordance with the European standard EN 14511–2:2018 [32] for low-temperature heating systems.

In the present experimental study, some parameters have been fixed:

- The fan velocity was fixed at 50% of the maximum speed;
- The high-pressure value was set at 80 bar;
- Photovoltaic modules were operated to achieve maximum power production.

The analysis of high-pressure and fan velocity effects has been carried out in a previous work [14], finding that when $T_{in,w}$ is equal to 30 °C and $T_{out,w}$ equal to 35 °C, the maximum COP is achieved with 80 bar of high-pressure and fan speed at 50%. Therefore, in the present tests the choice of 80 bar as high-pressure is made to achieve the highest values of COP. In addition, fixing the high-pressure levels allows the evaporation temperature (T_{evap}) to be used as a performance indicator for the heat pump: the higher the T_{evap}, the higher the Q_{GC} and the lower the P_c.

Table 2
Type B uncertainties of measured quantities and the main average combined uncertainties.

Sensor Type	Uncertainty	Main calculated quantities	Average combined uncertainty of calculated quantities
Thermocouples (T-type)	±0.1 K	Q_{GC}	± 1.4%
PT-100 sensor	1/10 DIN	COP_c	± 1.5%
Pressure sensor	±5 kPa	COP_{tot}	± 1.6%
Coriolis mass flow meter	0.1% of the reading		
Pyranometer, secondary standard	ISO 9060		
Power analyzer	0.1% of the reading		

Steady-state measurements were defined as those taken when high/low pressure remained within ±0.2 bar, the T_{air} stayed within ±1 K, and GTI was within ±30 W m^{-2}. Experimental data were recorded for 5 min once the heat pump achieved steady-state conditions, using a 10 s time step for data points, which were subsequently averaged.

3. Experimental results

Table 3 reports the experimental conditions of the tests conducted on the SA-DSHP during steady-state operation.

3.1. Solar-mode heat pump

PV-T evaporator performance is strictly linked to GTI and the $\dot{m}_r$ circulating in the collectors. In a previous study [33], several experimental tests were conducted on the same prototype without the use of a circulating pump. In the collectors, the $\dot{m}_r$ was guaranteed by natural circulation. Consequently, the $\dot{m}_r$ value was roughly constant in all the tests and it was observed that high superheating occurred at the outlet of the PV-T collector when GTI or compressor speed increased. The high degree of superheating at the collectors' outlet significantly decreased the T_{evap} and PV-T and heat pump performance [33]. In particular, the superheating at the collectors' outlet was due to an imbalance between the $\dot{m}_r$ circulating in the natural circulation loop of the PV-T collectors and the $\dot{m}_r$ processed by the compressor. To address this problem, a circulation pump was installed in the facility (Fig. 2) and preliminary tests were performed to determine the minimum speed to prevent the formation of superheated vapor at the collectors' outlet. Fig. 3 shows the degree of superheating measured at the PV-T collector outlet for different pump speed percentage values. The results refer to tests realized at the same compressor speed (75%), T_{air} (11.8 ± 0.5 °C) and GTI (933 ± 21 W m^{-2}). The superheating is the difference between the temperature measured at the collectors' outlet and T_{evap}. The data indicate that about 25 K of superheating occurs at the collector outlet when the pump speed is low (25%), while no superheating occurs at higher pump speeds (≥30%). Accordingly, 40% of the maximum pump speed was used for the subsequent tests as a preventive measure to ensure adequate $\dot{m}_r$ value to avoid superheating.

As mentioned above, the absence of superheating in the solar collectors positively affects their thermal efficiency (8). In this case, the efficiency is expressed as a function of the reduced temperature difference as proposed by Huang and Chyng [34]:

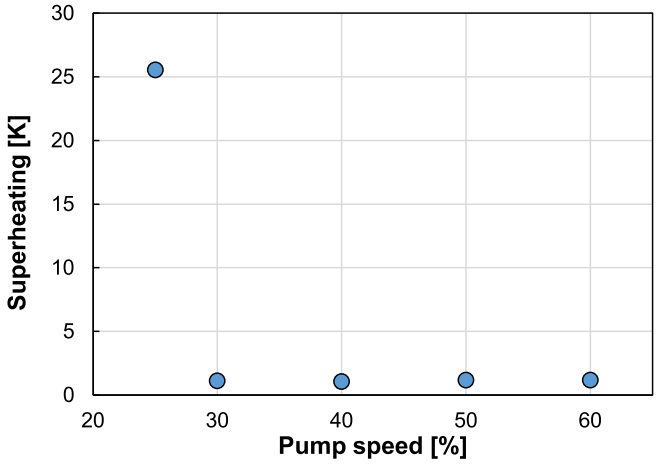

Fig. 3. Experimental values of superheating at the PV-T collectors' outlet for different pump speed. Tests in SOL-M at compressor speed equal to 75%, T_{air} of 11.8 °C and GTI of 933 W m^{-2}.

$$T_r = \frac{T_{evap} - T_{air}}{\mathrm{GTI}} \tag{9}$$

Fig. 4 shows the collector thermal efficiency values measured as a function of the reduced temperature difference for both natural and forced circulation. The data related to natural circulation are based on the results presented in a previous study [33]. When no vapor superheating occurs at the outlet of the PV-T collectors ($SH < 2$ K), the thermal efficiency values show a nearly linear downward trend, similar to the thermal efficiency curve of conventional solar thermal collectors. The present thermal efficiency displays values between 90% and 50%, when T_r goes from −0.03 to 0.005 K m^2 W^{-1}. On the contrary, in presence of superheating inside the PV-T collectors ($SH > 2$ K), thermal efficiency values are lower than those of the efficiency curve. In fact, the presence of superheating causes an increase in thermal losses to the environment. During forced circulation (new data in the present work), no superheating has been detected and the trend in thermal efficiency is in line with the results obtained with flooded collectors in natural

Table 3
Test conditions of the experimental campaign.

Evaporation mode	Number of tests	Compressor speed	High pressure	Fan velocity	Pump speed	T_{air}	GTI
[−]	[−]	[%]	[bar]	[%]	[%]	[°C]	[W m^{-2}]
AIR-M	27	40, 50, 75, 100	80	25, 50, 75, 100	/	11–17	/
SOL-M	14	40, 50, 75	80	/	40	10.5–19.6	500–1100
SIM-M	29	40, 50, 75, 100	80	50, 100	40	5.7–17.9	100–1100

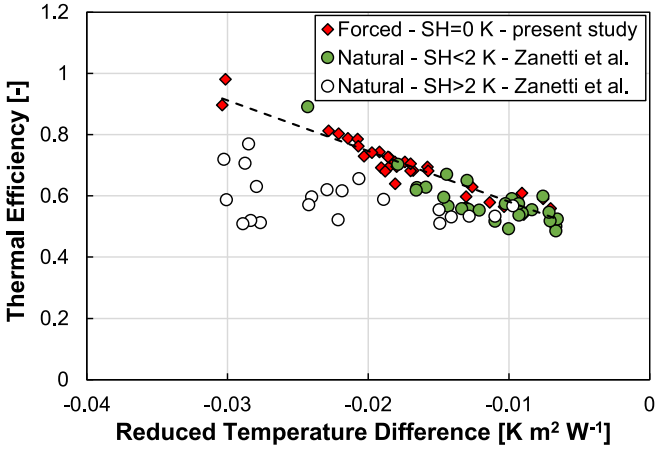

Fig. 4. Experimental PV-T collector thermal efficiency values versus reduced temperature difference. The results include the present measurements during forced circulation mode and those obtained by Zanetti et al. [33] during natural circulation mode with the superheating degree at the evaporator outlet.

circulation without superheating.

3.2. Simultaneous-mode heat pump

Fig. 5 shows the measured T_{evap} reached in the system, in steady-state condition, as a function of the GTI (Fig. 5a) and the T_{air} (Fig. 5b), obtained with the heat pump working in SOL-M and SIM-M at 50% of the maximum compressor speed.

In Fig. 5a, the tests were measured with T_{air} equal to 17.5 ± 0.3 °C in SIM-M and 16.4 ± 0.2 °C in SOL-M. The data show that, as GTI increases, T_{evap} also increases due to the higher useful heat for CO_2 evaporation in the PV-T collectors. In this range of GTI measurements (between 350 and 1100 W m^{-2}), T_{evap} increases almost linearly, but with a different slope between the two modes: 1.2 K every 100 W m^{-2} in SOL-M and about 0.6 K every 100 W m^{-2} in SIM-M. The increase in GTI has a smaller effect on T_{evap} in SIM-M compared to SOL-M because the refrigerant partially evaporates in the finned coil evaporator, which is not affected by the change in GTI. Regarding the Fig. 5b, during these tests, GTI was equal to 938 ± 27 W m^{-2} in SIM-M and 953 ± 29 W m^{-2} in SOL-M. Similarly to the results obtained at varying GTI, T_{evap} increases almost linearly with the T_{air}, but with a different slope. For an increment equal to 1 K in T_{air}, T_{evap} rises by 0.79 K in SIM-M and by 0.41 K in SOL-M. The variation of T_{air} has a more pronounced effect on T_{evap} in SIM-M than in SOL-M. In fact, the use of the finned coil evaporator coupled with the PV-T evaporator allows to better exploit the thermal sources.

An experimental comparison among the three different operation modes of the heat pump (AIR-M, SOL-M and SIM-M) was carried out at the same ambient conditions (T_{air} and GTI) and operative conditions (compressor speed, fan velocity, and pump speed). The results are presented in Fig. 6, where T_{evap} and the COP are reported for two different compressor speeds: 50% of the maximum speed (Fig. 6a) and 75% of the maximum speed (Fig. 6b). The operative conditions and the main results of the tests are summarized in Table 4.

For the tests in Fig. 6a, the average GTI was 1030 W m^{-2} with a deviation of ±10 W m^{-2} and the average T_{air} was 16.3 °C with a deviation of ±0.2 K. The results show that the SIM-M allows to achieve higher T_{evap}, outperforming air heat pump by 6.5 K and solar heat pump by 5.9 K. In fact, while T_{evap} in the SOL-M and in the AIR-M is mainly affected by GTI and T_{air}, respectively, T_{evap} in the SIM-M depends on both thermal sources, because its behavior is due to the combination of AIR-M and SOL-M operative modes. The higher T_{evap} is reflected in lower P_c (see Table 4) and in higher COP. Therefore, both COP_c and COP_{tot} are greater in the case of SIM-M. In particular, the COP_c is equal to 5.29 and it is 29% higher than AIR-M (COP_c equal to 4.10) and 28% higher than SOL-M (COP_c equal to 4.14). COP_{tot} is equal to 4.65 and it is 25% higher than AIR-M (COP_{tot} equal to 3.71) and 22% higher than SOL-M (COP_{tot} equal to 3.83). Table 4 shows also that, compared to the other two evaporation modes, the SIM-M operation not only allows a reduction in P_c (about −8%), but also an increase in Q_{GC} (about +18%), which explains the higher COP values.

With regards to the results reported in Fig. 6b, the average GTI was equal to 1020 W m^{-2} (±10 W m^{-2}) and the average T_{air} was equal to 15.2 °C (±0.2 K). The results show that, also at higher compressor speed, the SIM-M allows the achievement of higher T_{evap}, outperforming finned coil evaporation by 6.1 K and solar evaporation by 10.4 K. When operating in SOL-M, the amount of heat received by the PV-T evaporator is mainly dependent on the collector aperture area. Consequently, the reduction in T_{evap} that is observed at the higher compressor speed is attributed to the fact that the PV-T collectors' area is too small to evaporate this higher $\dot{m}_r$. Similar results were also found in [14,33]. The SIM-M addresses this issue, ensuring high heat pump performance even with an undersized PV-T plant. In SIM-M the COP_c is equal to 4.58, 21% higher than AIR-M (COP_c = 3.78) and 40% higher than SOL-M (COP_c = 3.28). Instead, the COP_{tot} is equal to 4.22, which is 19% higher than AIR-M (COP_{tot} = 3.53) and 36% higher than SOL-M (COP_{tot} = 3.11). As evident from Table 4, the SIM-M operation consistently demonstrates its effectiveness in optimizing energy efficiency by not only reducing P_c but also enhancing Q_{GC}. In particular, P_c is 5.5% lower than AIR-M and 8% lower than SOL-M, while Q_{GC} is 14% higher than AIR-M and 29% higher than SOL-M. In Table 4 the values of the photovoltaic power production (P_{PV}) are also reported for the SOL-M and SIM-M. The SOL-M enables the

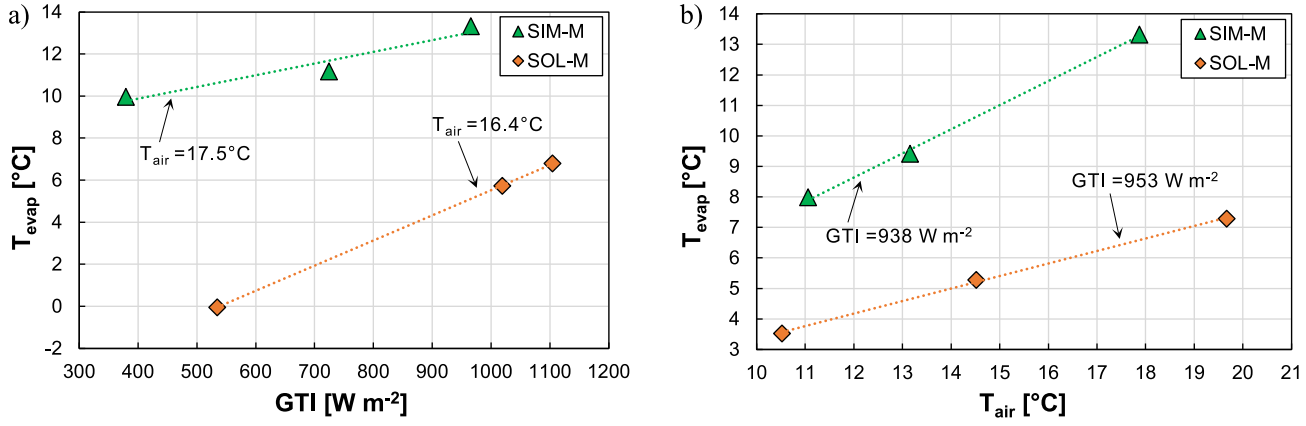

Fig. 5. Measured values of evaporation temperature (T_{evap}) when the heat pump works in SIM-M and SOL-M as a function of: a) GTI and b) T_{air}. Tests with 50% of the maximum compressor speed.

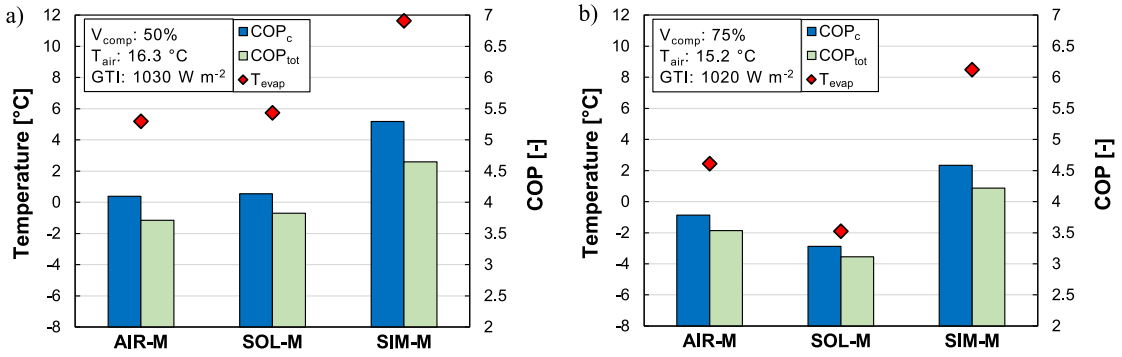

Fig. 6. Experimental comparison between AIR-M, SOL-M and SIM-M in terms of T_{evap} and COP. The results are based on tests carried out at a) 50% and b) 75% of the maximum compressor speed (V_{comp}).

Table 4
Summary of the main results during the experiments in steady-state operations.

Compr. speed	Evap. mode	GTI [W m^{-2}]	T_{air} [°C]	T_{evap} [°C]	P_{PV} [W]	P_c [W]	P_{tot} [W]	Q_{GC} [W]	COP_c [−]	COP_{tot} [−]
50%	AIR-M	–	16.5	5.2	–	603	667	2472	4.10	3.71
	SOL-M	1019	16.3	5.7	794	600	649	2483	4.14	3.83
	SIM-M	1039	16.2	11.6	781	551	612	2916	5.29	4.65
75%	AIR-M	–	15.1	2.5	–	968	1037	3663	3.78	3.53
	SOL-M	1018	15.4	−1.9	798	993	1045	3255	3.28	3.11
	SIM-M	1026	15.4	8.5	777	915	994	4191	4.58	4.22

production of slightly higher P_{PV} due to its lower T_{evap} and enhanced cooling of the PV cells.

4. Numerical model of the heat pump

4.1. Modelling of the components

The model of the heat pump (deployed using Matlab®) is used to evaluate the performance and energy fluxes in all environmental conditions and operative modes, both in steady-state and dynamic conditions. The model solves the supercritical CO_2 cycle and calculates the refrigerant thermodynamic conditions. Refprop 10.0 [30] is used to estimate the thermodynamic properties of CO_2, water and air. The model assumes that thermal losses and pressure drops are negligible in the heat exchangers, as well as in the compressor, and the throttling is isenthalpic.

The COMP model is based on three polynomial equations, depending on T_{evap}, the high-pressure and the compressor speed. Polynomial equations with the coefficients are reported in Zanetti et al. [35]. The heat exchangers models have been created taking into account a distributed parameter approach, where the energy, momentum and continuity equations are solved sequentially in each discretized element. The following models have already been described and validated against experimental data in previous works: the finned coil evaporator model [36], the PV-T evaporator model [33], the GC model [35] and the REC model [33].

The IHE model was created using the same procedure as the GC [35]. For the latter, the model inputs are:

- the geometry of the IHE;
- the mass flow rate $\dot{m}_r$ at the high-pressure side of the heat exchanger;
- the mass flow rate $\dot{m}_{r,l-p}$ at the low-pressure side of the heat exchanger;
- the refrigerant inlet temperature at the high-pressure side;
- the high-pressure and low-pressure;
- vapor quality at the outlet of the REC ($x_{in,l-p}$).

During the experiments, part of the mass flow rate exiting the receiver in the low-pressure side was directly by-passed to the compressor without entering the IHE, and for this reason a mass ratio r_{mass} between $\dot{m}_r$, at the high-pressure side, and $\dot{m}_{r,l-p}$ at the low-pressure side must be determined. This ratio, which depends on the aperture of the by-pass valve, has been determined experimentally and in the model the average value of 0.76 has been used. The IHE model has been validated against the experimental data collected in the operative conditions reported in Table 3. It predicts the heat flow rate exchanged on the high-pressure sides of the IHE with a mean absolute percentage deviation equal to 2.8% and with a maximum error equal to 12%.

4.2. Heat pump model algorithm

In Fig. 7 is reported the algorithm flowchart used in the model. The model requires different input values that concern the ambient conditions (as T_{air}, GTI and wind velocity), the operative conditions of the heat pump (as compressor speed, high-pressure, fan speed, water flow rate) and the electrical load associated with the PV modules array (MPPT can be selected alternatively). The refrigerant cycle solution algorithm is implemented by performing the following steps:

1. First tentative values of T_{evap} and superheating at the compressor suction (SH) are fixed at the beginning of a simulation.
2. $\dot{m}_r$, P_c and the isentropic compressor efficiency (η_{is}) are calculated through the compressor model. The isentropic compressor efficiency purpose is used to determine the enthalpy at the compressor discharge.
3. Q_{GC} and $T_{out,GC}$ are calculated through the GC model.
4. The refrigerant temperatures at the outlet of the IHE in the high-pressure ($T_{out,h-p}$) and low-pressure ($T_{out,l-p}$) side are calculated through the IHE model.
5. The procedure is repeated from point (2) to point (4) until the error between the calculated value and the guess value of the $T_{out,l-p}$ is higher than 0.01 K.
6. An updated value of the T_{evap} is then calculated, by solving the energy and mass equations in the REC. The mass balance is:

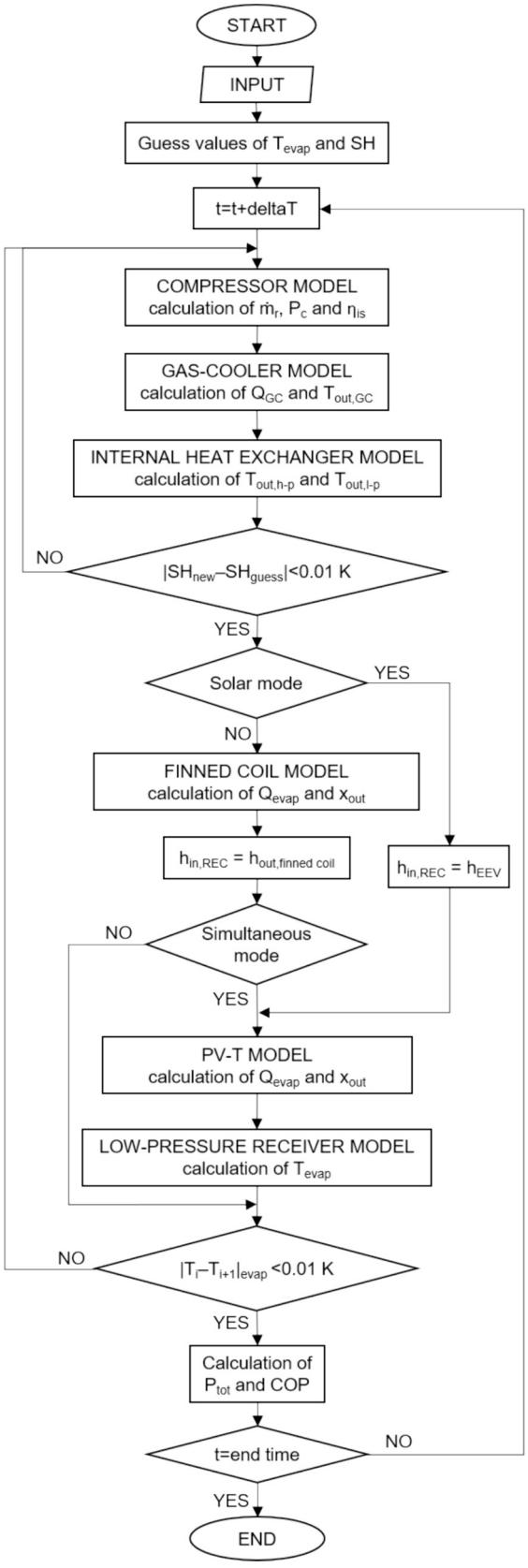

Fig. 7. HP model flowchart.

$$\frac{dm_{\mathrm{REC}}}{dt} = \frac{d}{dt}\left[\rho_l V_l + \rho_v (V_{\mathrm{REC}} - V_l)\right] \tag{10}$$

where V_{REC} and V_l are the volume, respectively, of the REC and of the CO_2 in liquid phase, ρ_l and ρ_v are the densities in liquid and vapor phases. In general, the variation of the refrigerant mass inside the REC depends on $\dot{m}_{\mathrm{COMP}}$ (which is the flow rate elaborated by the compressor) and of the flow rate circulating in the solar evaporator $\dot{m}_{\mathrm{PUMP}}$. It can be written in terms of enthalpy fluxes as:

$$\dot{m}_{COMP}\left(h_{\mathrm{in,REC}} - h_v\right) + \dot{m}_{\mathrm{PUMP}}\left(h_{\mathrm{PVT}} - h_l\right) = \frac{dH}{dt} \tag{11}$$

where H is the refrigerant total enthalpy in the REC and its rate of change depends on the liquid and vapor phases:

$$\frac{dH}{dt} = \frac{d}{dt}\left[\rho_l V_l h_l + \rho_v (V_{\mathrm{REC}} - V_l) h_v\right] \tag{12}$$

The left-side of Eq. (11) depends on the evaporative mode and it is evaluated in different ways:

a. When the heat pump works in SOL-M, only the PV-T model is used and, therefore $\dot{m}_{\mathrm{PUMP}} \neq 0$. The term h_l is the liquid-phase enthalpy at the inlet of the PV-T evaporator, h_{PVT} is the enthalpy at the outlet of the PV-T evaporator and it is calculated by the PV-T model, while $h_{in,\mathrm{REC}}$ is the enthalpy at the outlet of the EEV (h_{EEV}) which is known according to the previous steps.
b. When the heat pump works in AIR-M, only the finned coil model is used and, therefore $\dot{m}_{\mathrm{PUMP}} = 0$. The term $h_{in,\mathrm{REC}}$ is the enthalpy at the outlet of the finned coil evaporator and it is determined by the finned coil model.
c. When the heat pump works in SIM-M, the finned coil model is used first and then the PV-T model. The same terms of point (a) are assumed, except for $h_{in,\mathrm{REC}}$ which now is the enthalpy at the outlet of the finned coil evaporator.

To summarize, the evaporator models calculate the values of enthalpy and vapor quality x_{out} at the inlet of the REC, while the REC model calculates T_{evap}.

7. The procedure is repeated from point (2) to point (6) until the T_{evap} reaches a convergence value within a tolerance of 0.01 K. Then the COP is calculated.

After the iterative procedure, the heat pump COP operating in steady-state conditions is evaluated. The model can also evaluate the heat pump dynamic operation when the environmental conditions change at each time step.

5. Numerical results

5.1. Comparison with the experimental data

The heat pump numerical model has been validated both in steady-state and dynamic operation.

Fig. 8 presents a comparison between the model's predicted results and the experimental data collected in steady-state (refer to Table 3), for SIM-M and SOL-M. The COP_{tot} (a), the Q_{GC} (b) and the P_{tot} (c), calculated using this model are within error bands of ±5%. Regarding the T_{evap}, the average absolute error is equal to 0.74 K in SOL-M and 0.57 K in SIM-M.

Fig. 9 shows the dynamic validation of the model when the heat pump is working in SOL-M. The experimental data and the numerical values of T_{evap} (Fig. 9b) are compared during a partly cloudy day with both T_{air} and GTI varying with time (Fig. 9a). During the test, 50% of the maximum compressor speed and 30% of the maximum pump speed were set. It can be noticed that, according to the steady state outcomes, the T_{evap} follows the GTI trend, but its variation is damped by the

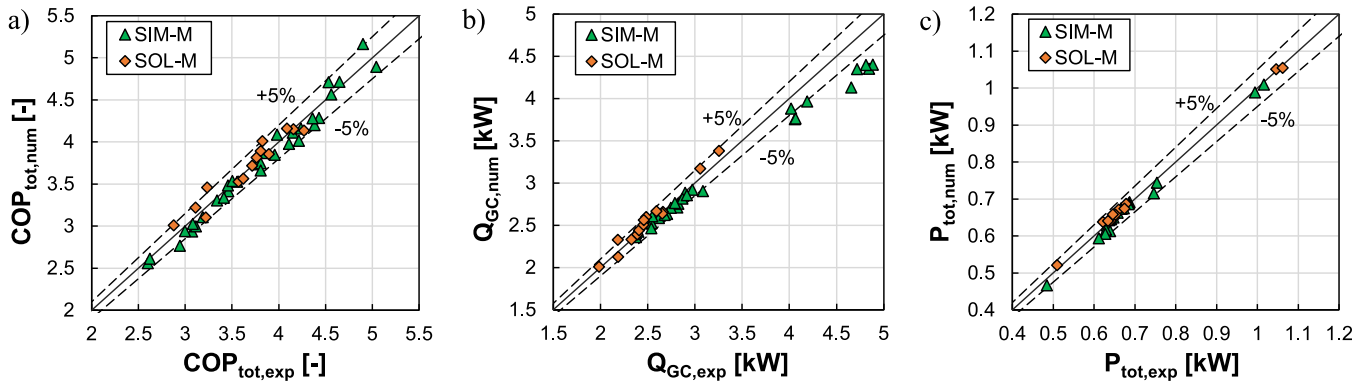

Fig. 8. Comparison between the numerical (num) and experimental (exp) values of: a) COP_{tot}, b) Q_{GC} and c) P_{tot}. Data refer to steady-state tests in both SIM-M and SOL-M.

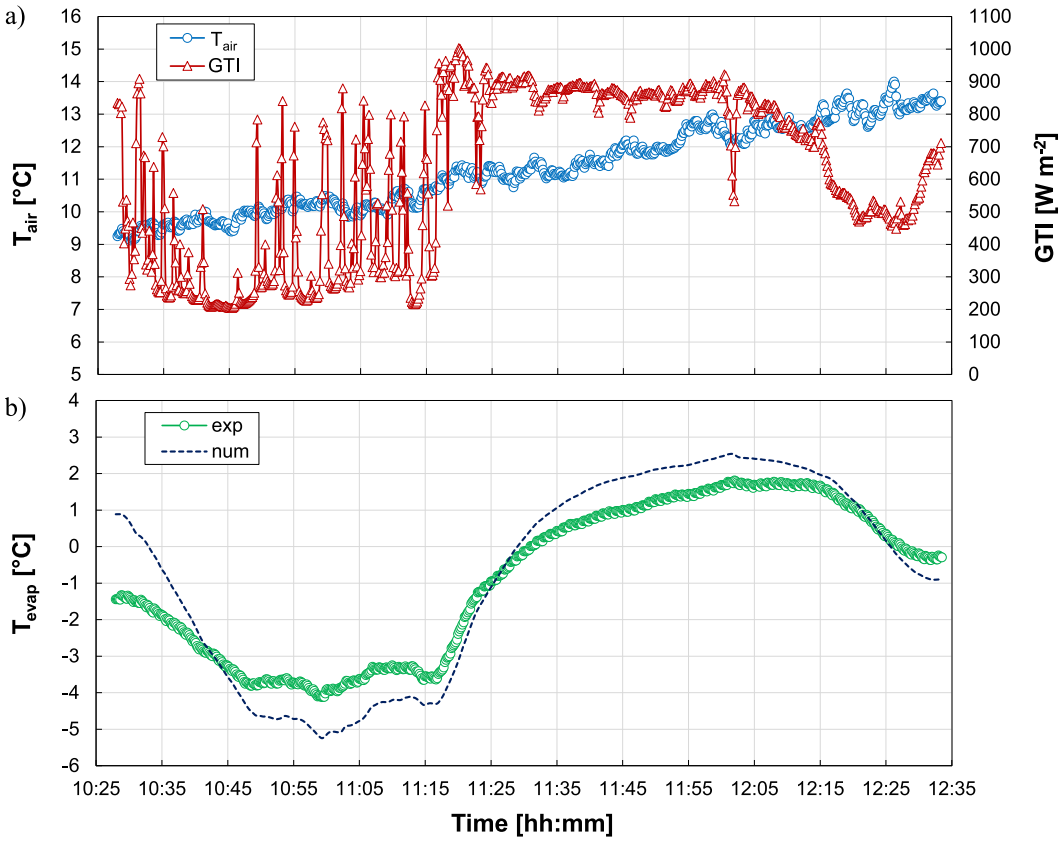

Fig. 9. a) Experimental values of T_{air} and GTI: input for the calculation reported in b). b) Experimental (exp) and numerical (num) evolution of the T_{evap} obtained in SOL-M during a dynamic test.

thermal inertia of the PV modules. Between 10:30 and 11:15, as the clouds passed over the PV-T collectors and the available solar radiation decreased (with an average GTI of 270 W m^{-2}), the evaporation temperature T_{evap} decreased. In particular, the measured and predicted evaporation temperatures stabilized at about −3.5 °C and − 4.5 °C, respectively. After the passage of the clouds, the GTI rose to around 870 W m^{-2}, resulting in an increased useful heat for evaporating the CO_2 in the collectors. At the same time, the increasing air temperature also provides more thermal energy for the finned coil evaporator. As a result, the evaporation temperature increases. The highest measured T_{evap} was 1.8 °C, which is slightly lower than the predicted value of 2.5 °C. Overall, the model can predict the response of the SA-DSHP with good accuracy and the average error in T_{evap} is lower than 1 K.

5.2. Heat pump dynamic response

The validated dynamic model allows a comparison of the heat pump performance in the three different evaporation modes under the same operating and environmental conditions. The fixed operating conditions are: compressor and fan speed at 50%, high-pressure at 80 bar, water heated from 30 °C to 35 °C.

Fig. 10 displays the T_{evap} (a), the Q_{GC} (b), P_{tot} (c) and d) COP_{tot} predicted by the model during air, solar and simultaneous evaporation mode at the same environmental conditions shown in Fig. 9a. These operative conditions are interesting because they are representative of a partly cloudy day: in the first hour GTI is around 300 W m^{-2} and in the second hour it increases up to 900 W m^{-2} before decreasing again down to 500 W m^{-2}; during the test, T_{air} presents a quasi-linear increase from

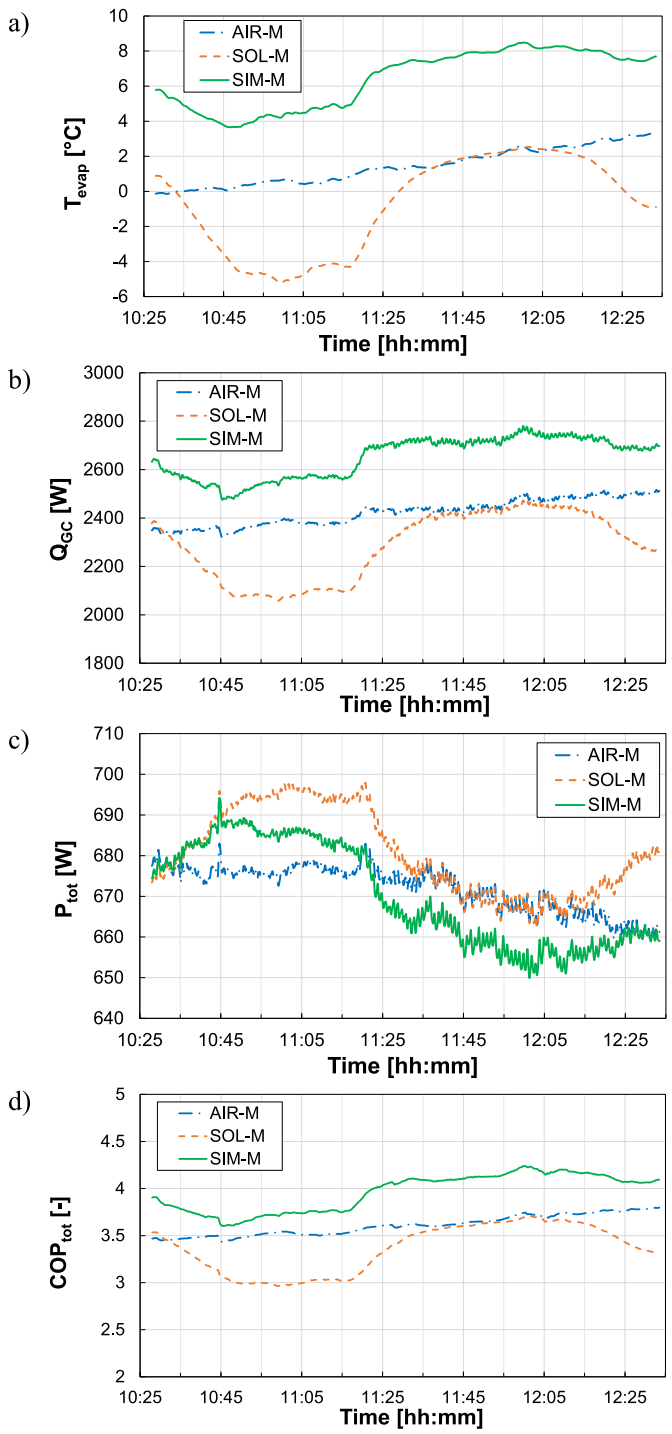

Fig. 10. Comparison between a) T_{evap}, b) Q_{GC}, c) P_{tot} and d) COP_{tot} predicted by the model for AIR-M, SOL-M and SIM-M. The input T_{air} and GTI values are reported in Fig. 9a.

9 °C up to 13 °C. Considering Fig. 10a, in AIR-M, T_{evap} increases with time following the same trend shown by T_{air} in Fig. 9a. On the other hand, in SOL-M, T_{evap} is strongly influenced by GTI and it varies as a consequence of a GTI variation (as reported in Fig. 9a). Interestingly, the SIM-M produces a higher T_{evap}, compared to the other two modes, in all the considered conditions. For instance, from 10:35 to 11:15, when T_{air} is between 9 °C and 10.5 °C and the mean GTI is equal to 353 W m^{-2} (see Fig. 9a), the value of T_{evap} in AIR-M is higher than that in SOL-M (the maximum difference between the two temperatures is equal to 5.8 K), while the SIM-M outperforms the other two with a mean T_{evap} equal to 4.3 °C. In this operative condition, even if GTI is very low, the SIM-M allows to reach a higher T_{evap}, and thus higher performance, compared to the AIR-M. Another interesting comparison can be drawn considering the results from 11:35 to 12:05, obtained with T_{air} between 11 °C and 13 °C and a GTI between 850 W m^{-2} and 900 W m^{-2} (see Fig. 9a). The values of T_{evap} in AIR-M and SOL-M are similar (from 1.3 °C to 2.4 °C), while in SIM-M T_{evap} is about 6 K higher.

Looking at Fig. 10b, Q_{GC} has the same trend as T_{evap} and, thus, the SIM-M produces always higher values than the other two modes. As previously observed for T_{evap}, it can be seen that from 11:35 to 12:05 both the AIR-M and SOL-M provide the same Q_{GC}, about 2450 W. However, the SIM-M provides a Q_{GC} of about 2700 W. P_{tot} of the HP for the three different modes (Fig. 10c), generally, has values with an opposite trend compared to that of T_{evap} because the pressure ratio, at the compressor, decreases when T_{evap} increases, due to the fixed value of the high-pressure. When considering P_c, the differences among the three operative modes are <3%. Although in SIM-M T_{evap} is consistently higher than in AIR-M, P_{tot} is about 2% lower compared to the AIR-M only when GTI is high (>600 W m^{-2}), whereas, with a cloudy sky, it is always higher (about 1.5%). On the other hand, compared to the SOL-M, P_{tot} in SIM-M is always lower. According to Fig. 10a and Fig. 10b, it is observed that from 11:35 to 12:05 both the AIR-M and SOL-M exhibit the same P_{tot} in Fig. 10c.

Finally, in Fig. 10d the trends in COP_{tot} values reflect the trends in Q_{GC}. The COP_{tot} in SIM-M fluctuates between 3.6 and 4.2, and its values are always higher than AIR-M (values between 3.5 and 3.8) and SOL-M (values between 3.0 and 3.7).

5.3. Control strategy

The developed numerical model allows comparing the three different evaporation modes under the same environmental and operational constraints, in order to analyze the heat pump performance. As seen from the experimental data (3.2), the performance is affected only by air temperature when operating with the finned coil evaporator. Conversely, when utilizing the PV-T evaporator, the performance is predominantly dependent on solar irradiance and, to a lesser extent, on air temperature.

Fig. 11 shows the results of steady-state simulations obtained with the heat pump operating in AIR-M, SOL-M and SIM-M when T_{air} is equal to 0 °C (a, c and e) or to 15 °C (b, d and f) and GTI varies between 500 W m^{-2} and 1200 W m^{-2}. The operating conditions are: compressor and fan speed at 50%, pump speed at 40%, high-pressure at 80 bar, water heated from 30 °C to 35 °C.

When T_{air} is equal to 0 °C (Fig. 11a), T_{evap} in SOL-M is higher than that in AIR-M if GTI exceeds 600 W m^{-2}. When the heat pump operates in SIM-M, it can achieve higher T_{evap} than SOL-M until its value is lower than 0 °C. This crossing point is reached at a very high GTI equal to 1050 W m^{-2}. This happens because, when T_{evap} becomes higher than T_{air}, the contribution of air as heat source is negative and this penalizes the performance of the SIM-M compared to the SOL-M.

When T_{air} is equal to 15 °C (Fig. 11b), T_{evap} in SIM-M is always higher than AIR-M and SOL-M whatever GTI values. In fact, according to the outcomes of Fig. 11a, T_{evap} never exceeds T_{air}. On the contrary, T_{evap} in SOL-M is higher than that in AIR-M only when GTI is higher than 900 W m^{-2}.

Fig. 11c and d show the calculated COP_{tot} when T_{air} is equal to 0 °C and to 15 °C, respectively. Generally, the COP_{tot} trend follows those of T_{evap}. In SIM-M, the COP_{tot} increases with GTI (from 3 to 3.34 and from 4.28 to 4.88 when T_{air} is 0 °C and 15 °C, respectively), but with a slope lower than that of the SOL-M and always higher than that of the AIR-M. At 0 °C of T_{air} (Fig. 11c), the SIM-M provides a higher COP_{tot} than SOL-M until GTI is lower than 900 W m^{-2}, corresponding to a COP_{tot} of 3.2. This crossing point is situated at a lower GTI than the one identified for T_{evap} and the reason is that P_{tot} of the heat pump in SIM-M exceeds that in SOL-M.

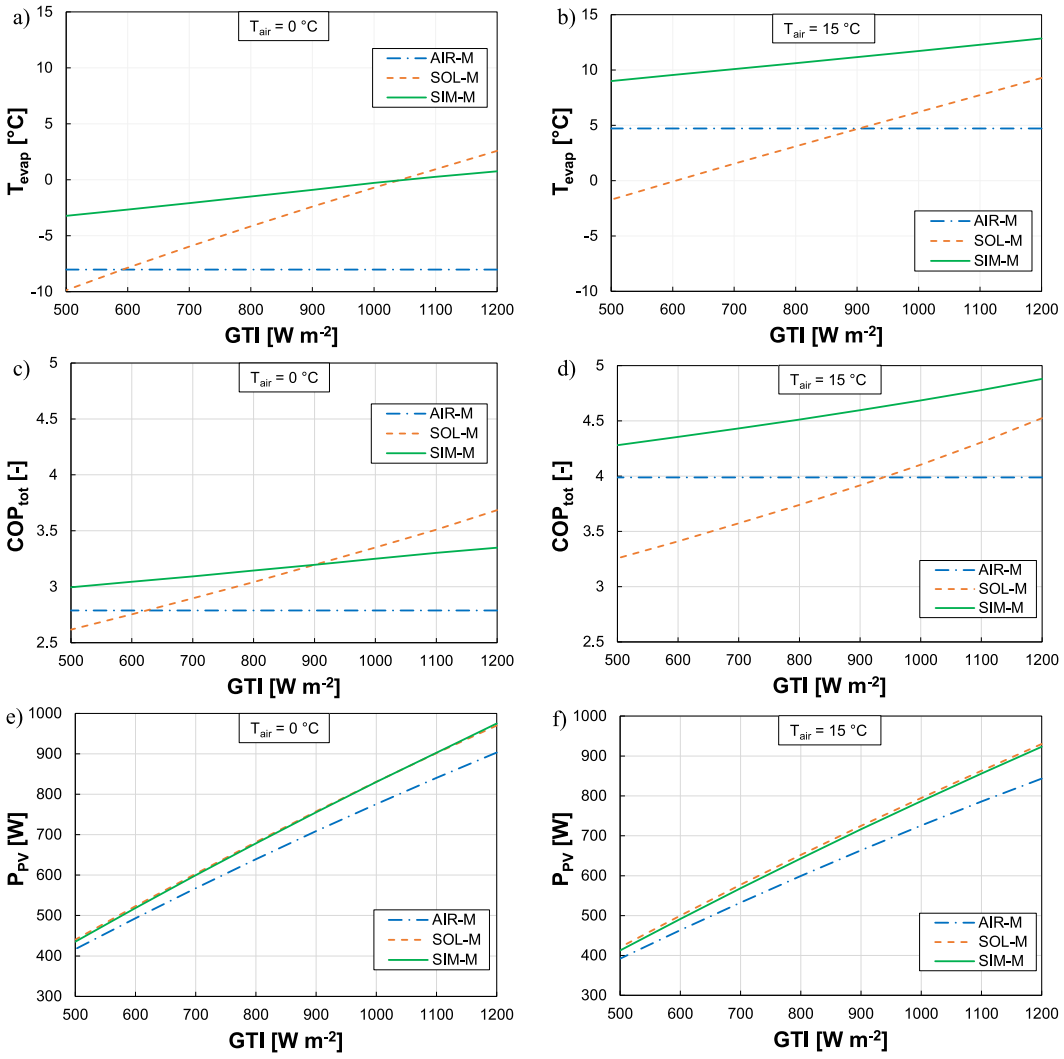

Fig. 11. Simulation of the effect of GTI on T_{evap} (a, b), COP_{tot} (c, d) and P_{PV} (e, f) at two different T_{air} values. Comparison between the AIR-M, SOL-M and SIM-M at 50% of the maximum compressor speed.

Fig. 11e and f show the calculated P_{PV} when T_{air} is equal to 0 °C and to 15 °C, respectively. The P_{PV} increases when increasing GTI and decreasing T_{air}. The SOL-M and SIM-M produce the same P_{PV}, which is higher than that produced in AIR-M due to the cooling effect of the refrigerant on the photovoltaic cells. At 0 °C of T_{air} (Fig. 11e), this increase is between 4.4% at 500 W m^{-2} and 8.0% at 1200 W m^{-2}, while at 15 °C of T_{air} (Fig. 11f), this increase is between 5.3% at 500 W m^{-2} and 9.5% at 1200 W m^{-2}. This P_{PV} increase corresponds to an improvement of the PV conversion efficiency from 15% to 16.2%.

Considering the present results, if the heat pump operated in either AIR-M or SOL-M, a control algorithm should be implemented in the heat pump software, to decide which heat source to use according to the parameter that has to be optimized (e.g. COP_{tot}). The controller should be capable of continuously monitoring and predicting the heat pump's performance in response to dynamic environmental and operational variables and decide if it is necessary to switch between the thermal sources to avoid excessive switching, particularly on partially cloudy days or when there are sudden changes in T_{air}. The use of the SIM-M can avoid or limit the number of times the control algorithm operates and can guarantee, in a broad range of operative conditions, maximum performance.

In the next Section, the model is used to predict the impact of varying the number of solar collectors.

5.4. Optimal design of the system

The numerical model can also be used as a design tool. In this study, it was considered useful to examine how changing the number of PV-T collectors ($N_{PV\text{-}T}$) impacts the HP performance. Indeed, increasing or decreasing $N_{PV\text{-}T}$ means modifying the evaporator area in either SOL-M or SIM-Ms. Similar to the effect of GTI (see Fig. 11), increasing $N_{PV\text{-}T}$ is beneficial to the SOL-M as T_{evap} in the system increases. On the other hand, the increased $N_{PV\text{-}T}$ may lead the SOL-M to outperform the one operating in SIM-M (Fig. 11).

Fig. 12 displays the relationship between T_{evap} and COP_{tot} versus $N_{PV\text{-}T}$ in SIM-M and SOL-M, considering three different GTI levels (1200, 900 and 500 W m^{-2}). The numerical results are also compared with the values of T_{evap} and COP_{tot} obtained for the AIR-M, when the T_{air} is 0 °C (Fig. 12a and Fig. 12c, respectively) and 15 °C (Fig. 12b and Fig. 12d, respectively). Throughout the simulation, the compressor and pump speeds were held constant at 50% and 40% of their maximum speed, respectively.

At 0 °C T_{air} (Fig. 12a), T_{evap} in SIM-M increases roughly linearly with the number of PV-T collectors, due to the increased collector absorbing surface. This result is independent of GTI. In comparison with the SOL-M, it is advantageous to increase the $N_{PV\text{-}T}$ in SIM-M until T_{evap} reaches values equal to T_{air}. Over this value, the finned coil cannot work as an evaporator and T_{evap} will be lower than that realized in SOL-M. The

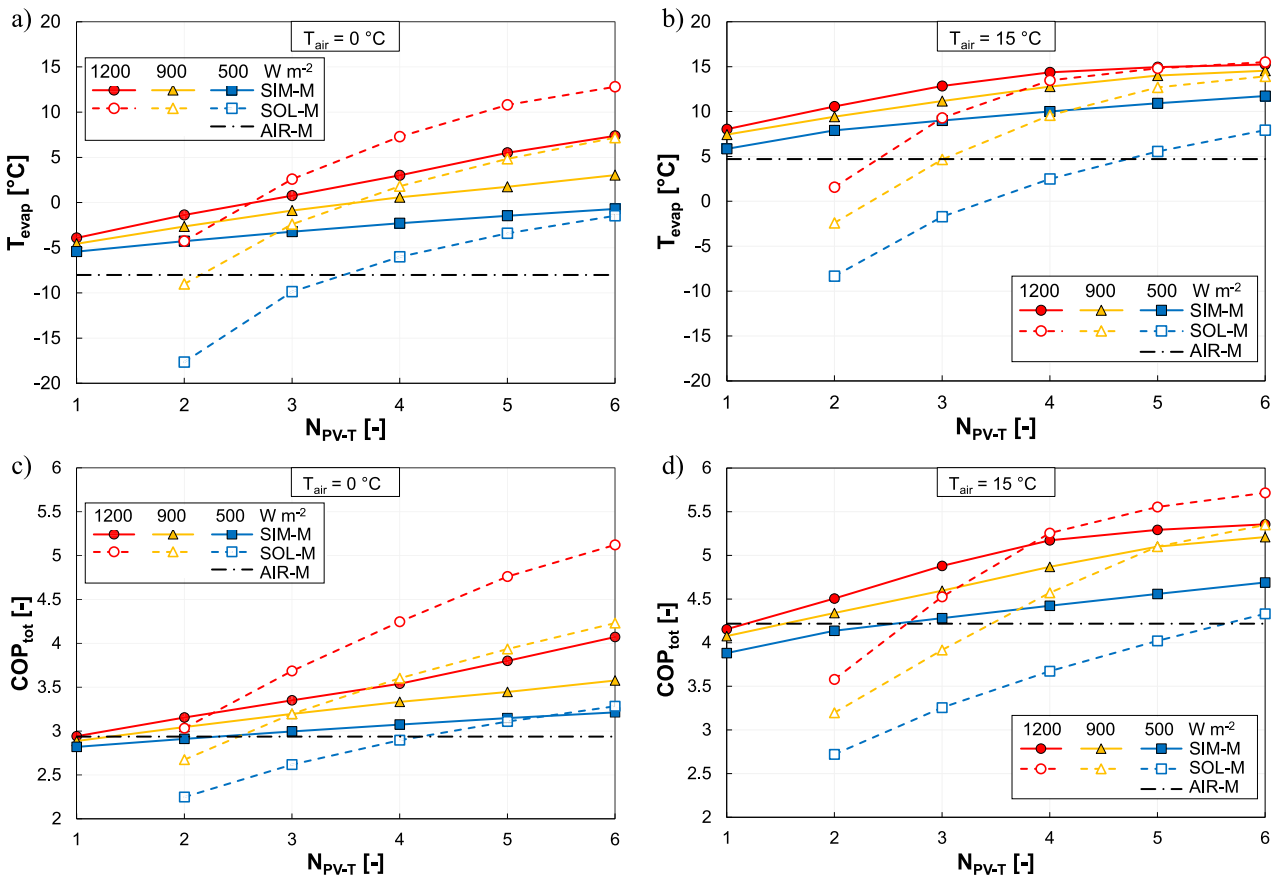

Fig. 12. Effect of number of PV-T collectors ($N_{PV\text{-}T}$) on the T_{evap} (a, b) and COP_{tot} (c, d) calculated by the developed model for the three different working modes (SIM-M, SOL-M and AIR-M) at a) 0 °C and b) 15 °C air temperature. The results refer to different GTI values (500, 900 and 1200 W m^{-2}) and 50% of the maximum compressor speed.

maximum $N_{PV\text{-}T}$ to have higher T_{evap} in SIM-M compared to SOL-M is 2 for GTI of 1200 W m^{-2} or 3 for GTI of 900 W m^{-2}. Similar considerations can also be drawn for T_{air} equal to 15 °C (Fig. 12b). The higher the T_{air}, the greater the contribution of the finned coil evaporator to the evaporation process. Therefore, the maximum $N_{PV\text{-}T}$ for achieving better performance in SIM-M with respect to SOL-M increases compared to the case at lower T_{air} (Fig. 12a), and it is equal to 5 when GTI is 1200 W m^{-2} and 6 when the GTI is 900 W m^{-2}.

The T_{evap} increase leads to a corresponding increase in COP_{tot} with a similar trend. As compared to the AIR-M, it can be noted that, for both low (Fig. 12a) and high (Fig. 12b) T_{air} values, the SIM-M allows evaporation at higher temperatures also when only one PV-T collector is installed. This is not true for the COP_{tot}, which requires at least 2 PV-T collectors to provide a higher value in SIM-M compared to the AIR-M.

To conclude, the use of a SA-DSHP in SIM-M proves to be more advantageous in terms of T_{evap} compared to the AIR-M, regardless of GTI and T_{air}. This advantage is valid even with only one PV-T collector installed and increases with the $N_{PV\text{-}T}$. However, in terms of COP_{tot} the SIM-M is advantageous with at least two PV-T collectors installed. Of course, as a guideline for the design, the proper solar collector area must be related to the capacity of the heat pump. On the other hand, when a high $N_{PV\text{-}T}$ is installed, the use of the SIM-M can perform worse than the SOL-M. As a rule of thumb, the switch convenience point from SIM-M to SOL-M can be appropriately identified when the T_{evap} is about equal to T_{air}. Furthermore, in applications with limited available surface space, the installation of a SA-DSHP operating in SIM-M allows for a compact design with good performance.

6. Concluding remarks

This study presents an experimental prototype and numerical model of a novel dual-source solar-air heat pump utilizing CO_2 as a refrigerant. The key innovation lies in the combined operation of two evaporators, the finned-coil and the PV-T collector, enabling selection between air and solar energy or their simultaneous use.

Experimental results confirm the effectiveness of this approach. Simultaneous-mode operation demonstrably outperforms air and solar-only modes, achieving significantly higher evaporation temperatures (up to 10 K increase) and improved coefficient of performance (COP) (up to 36% increase).

A validated numerical model further underscores the advantages of simultaneous operation. It predicts superior performance until the air temperature surpasses the evaporation temperature, at which point solar-only mode becomes preferable. Additionally, the model suggests that increasing the number of PV-T collectors enhances performance in simultaneous-mode, especially at higher air temperatures.

This research paves the way for a more efficient and adaptable heat pump design. The dual-source solar-air concept operating in simultaneous-mode, even in applications with limited solar area, enables the achievement of improved performance as compared to a mere air-source installation and maximizes the utilization of renewable sources for space heating applications. Future developments will focus on the usage of the present heat pump in other seasons, both for domestic hot water production and for investigating the PV/T solar assisted concept in air conditioning applications.

Nomenclature

Abbreviations

AIR-M	Air-mode
ASHP	Air source heat pump
COMP	Compressor
COP	Coefficient of performance
DX-SAHP	Direct-expansion solar-assisted heat pump
EEV	Electronic expansion valve
EVAP	Evaporator
GC	Gas-cooler
IHE	Internal heat exchanger
MPPT	Maximum power point tracking
PUMP	Circulation pump
PV	Photovoltaic
PV-T	Photovoltaic-thermal solar collector
REC	Low-pressure receiver
SAHP	Solar-assisted heat pump
SA-DSHP	Solar-air dual-source heat pump
SIM-M	Simultaneous-mode
SOL-M	Solar-mode

Symbols

A	Area [m^2]
c	Specific heat capacity [J kg^{-1} K^{-1}]
GTI	Global tilted irradiance [W m^{-2}]
h	Specific enthalpy [J kg^{-1}]
H	Total enthalpy [J]
$\dot{m}$	Mass flow rate [kg s^{-1}]
P	Electrical Power [W]
SH	Superheting
Q	Heat flow rate [W]
T	Temperature [°C]
V	Volume [m^3]
x	Vapor quality [−]
η	Efficiency [−]
ρ	Density [kg m^{-3}]

Subscripts

c	Compressor
$h\text{-}p$	High-pressure
in	Inlet
l	Liquid
$l\text{-}p$	Low-pressure
out	Outlet
r	Refrigerant
tot	Total
v	Vapor
w	Water

CRediT authorship contribution statement

Riccardo Conte: Writing – original draft, Validation, Software, Investigation, Formal analysis. **Emanuele Zanetti:** Writing – review & editing, Software, Investigation. **Marco Tancon:** Writing – review & editing, Writing – original draft, Visualization, Investigation, Formal analysis, Data curation. **Marco Azzolin:** Writing – review & editing, Supervision, Methodology, Conceptualization. **Sergio Girotto:** Writing – review & editing, Resources. **Davide Del Col:** Conceptualization, Funding acquisition, Supervision, Writing – review & editing.

Declaration of competing interest

The authors declare the following financial interests/personal relationships which may be considered as potential competing interests:

This study was developed in the framework of the research activities carried out within the Project "Network 4 Energy Sustainable Transition—NEST", Spoke 1., Project code PE0000021, funded under the National Recovery and Resilience Plan (NRRP), Mission 4, Component 2, Investment 1.3— Call for tender No. 1561 of 11.10.2022 of Ministero dell'Universita`e della Ricerca (MUR); funded by the European Union—NextGenerationEU.

Data availability

Data will be made available on request.

Acknowledgements

This study was developed in the framework of the research activities carried out within the Project "Network 4 Energy Sustainable Transition—NEST", Spoke 1., Project code PE0000021, funded under the National Recovery and Resilience Plan (NRRP), Mission 4, Component 2, Investment 1.3 — Call for tender No. 1561 of 11.10.2022 of Ministero dell'Universita`e della Ricerca (MUR); funded by the European Union—NextGenerationEU.

References

[1] Wang X, Xia L, Bales C, Zhang X, Copertaro B, Pan S, et al. A systematic review of recent air source heat pump (ASHP) systems assisted by solar thermal, photovoltaic and photovoltaic/thermal sources. Renew Energy 2020;146:2472–87.
[2] Kropas T, Streckienė G, Bielskus J. Experimental investigation of frost formation influence on an air source heat pump evaporator. Energies 2021;14.
[3] Song M, Deng S, Dang C, Mao N, Wang Z. Review on improvement for air source heat pump units during frosting and defrosting. Appl Energy 2018;211:1150–70.
[4] Kamel RS, Fung AS, Dash PRH. Solar systems and their integration with heat pumps: a review. Energ Buildings 2015;87:395–412.
[5] Zhou J, Zeng C, Wang Z, Lyu W, Tang Y, Wu D, et al. Indirect expansion solar assisted heat pump system: a review. Sustain Energy Technol Assess 2022;53:102409.
[6] Faisal Ahmed S, Khalid M, Vaka M, Walvekar R, Numan A, Khaliq Rasheed A, et al. Recent progress in solar water heaters and solar collectors: a comprehensive review. Therm Sci Eng Progress 2021;25:100981.
[7] Cerit E, Erbay LB. Investigation of the effect of rollbond evaporator design on the performance of direct expansion heat pump experimentally. Energ Conver Manage 2013;72:163–70.
[8] Sun X, Wu J, Dai Y, Wang R. Experimental study on roll-bond collector/evaporator with optimized-channel used in direct expansion solar assisted heat pump water heating system. Appl Therm Eng 2014;66:571–9.
[9] Kong X, Sun P, Dong S, Jiang K, Li Y. Experimental performance analysis of a direct-expansion solar-assisted heat pump water heater with R134a in summer. Int J Refrig 2018;91:12–9.
[10] Yu X, Guo Z, Gao Z, Yang B, Ma X, Dong S. Thermodynamic investigation of a direct-expansion solar assisted heat pump with evacuated tube collector-evaporator. Renew Energy 2023;206:418–27.
[11] Sezen K, Gungor A. Comparison of solar assisted heat pump systems for heating residences: a review. Solar Energy 2023;249:424–45.
[12] Shi GH, Aye L, Li D, Du XJ. Recent advances in direct expansion solar assisted heat pump systems: a review. Renew Sustain Energy Rev 2019;109:349–66.
[13] Shao N, Ma L, Zhang J. Experimental investigation on the performance of direct-expansion roof-PV/T heat pump system. Energy 2020;195:116959.
[14] Zanetti E, Azzolin M, Girotto S, Del Col D. Performance and control of a CO2 dual source solar assisted heat pump with a photovoltaic-thermal evaporator. Appl Therm Eng 2023;218.
[15] Simonetti R, Moretti L, Molinaroli L, Manzolini G. Energetic and economic optimization of the yearly performance of three different solar assisted heat pump systems using a mixed integer linear programming algorithm. Energ Conver Manage 2020;206:112446.
[16] Li J, Wei S, Dong Y, Liu X, Novakovic V. Technical and economic performance study on winter heating system of air source heat pump assisted solar evacuated tube water heater. Appl Therm Eng 2023;221:119851.
[17] Li T, Liu Q, Wang X, Gao J, Li G, Mao Q. A comprehensive comparison study on household solar-assisted heating system performance in the hot summer and cold winter zone in China. J Clean Prod 2024;434:140396.
[18] Deng W, Yu J. Simulation analysis on dynamic performance of a combined solar/air dual source heat pump water heater. Energ Conver Manage 2016;120:378–87.

[19] Li Z, Huang X. Simulation analysis on operation performance of a hybrid heat pump system integrating photovoltaic/thermal and air source. Appl Therm Eng 2022;200:117693.
[20] Li S, Yang H, Yuan J, Zeng X, Yang Z, Lu J. Thermodynamic and economic analyses of modified ejector enhanced solar-air composite dual-source heat pump system in residential buildings. Energ Buildings 2024;308.
[21] Cai J, Li Z, Ji J, Zhou F. Performance analysis of a novel air source hybrid solar assisted heat pump. Renew Energy 2019;139:1133–45.
[22] Cai J, Zhang F, Ji J. Comparative analysis of solar-air dual source heat pump system with different heat source configurations. Renew Energy 2020;150:191–203.
[23] Yang H, Wang X, Yao S. Thermodynamic analysis of a novel solar photovoltaic thermal collector coupled with switchable air source heat pump system. Appl Therm Eng 2023;218.
[24] Zhang Y, Ji J, Song Z, Ke W, Xie H. Performance prediction on a novel dual-mode heat pump with a hybrid photovoltaic/micro-channel heat pipe/fin heat exchanger. Energ Conver Manage 2023;293.
[25] James A, Srinivas M, Mohanraj M, Raj AK, Jayaraj S. Experimental studies on photovoltaic-thermal heat pump water heaters using variable frequency drive compressors. Sustain Energy Technol Assess 2021;45:101152.
[26] Zhou J, Zhao X, Ma X, Qiu Z, Ji J, Du Z, et al. Experimental investigation of a solar driven direct-expansion heat pump system employing the novel PV/micro-channels-evaporator modules. Appl Energy 2016;178:484–95.
[27] Rabelo SN, Paulino TF, Duarte WM, Maia AAT, Machado L. Experimental analysis of the influence of the expansion valve opening on the performance of the small size CO2 solar assisted heat pump. Solar Energy 2019;190:255–63.
[28] EU No 2024/573. Regulation (EU) 2024/573 of the European Parliament and of the Council of 7 February 2024 on fluorinated greenhouse gases, amending Directive (EU) 2019/1937 and repealing Regulation (EU) No 517/2014. Off J Eur Union 2024.
[29] Song Y, Cui C, Yin X, Cao F. Advanced development and application of transcritical CO2 refrigeration and heat pump technology—a review. Energy Rep 2022;8:7840–69.
[30] Lemmon EW, Huber ML, Mclinden MO. REFPROP 10.0, NIST Standard Reference Database. 2018.
[31] Joint Committee for Guides in Measurements. Evaluation of measurement data — Guide to the expression of uncertainty in measurement. International Organization for Standardization Geneva ISBN; 2008.
[32] EN 14511–-2:2018. Air Conditioners, Liquid Chilling Packages and Heat Pumps for Space Heating and Cooling and Process Chillers, with Electrically Driven Compressors - Part 2: Test Conditions. 2018.
[33] Zanetti E, Azzolin M, Conte R, Girotto S, Del Col D. Experiments and dynamic modelling of dry expansion and flooded evaporators in a CO2 solar assisted heat pump. Appl Therm Eng 2022;217.
[34] Huang BJ, Chyng JP. Performance characteristics of integral type solar-assisted heat pump. Solar Energy 2001;71:403–14.
[35] Zanetti E, Bordignon S, Conte R, Bisi A, Azzolin M, Zarrella A. Experimental and numerical analysis of a CO2 dual-source heat pump with PVT evaporators for residential heating applications. Appl Therm Eng 2023;233:121165.
[36] Zanetti E, Bonduà S, Bortolin S, Bortolotti V, Azzolin M, Tinti F. Sequential coupled numerical simulations of an air/ground-source heat pump: validation of the model and results of yearly simulations. Energ Buildings 2022;277:112540.
[37] ISO9060, Solar energy — Specification and classification of instruments for measuring hemispherical solar and direct solar radiation, *International Organization for Standardization*, 2018.